Optical properties of alkali-metal atoms in pressurized liquid helium

T. Kinoshita, K. Fukuda, Y. Takahashi, and T. Yabuzaki
Department of Physics, Faculty of Science, Kyoto University, Kyoto 606-01, Japan
(Received 13 March 1995)

The excitation and emission spectra of alkali-metal atoms (Cs and Rb) in liquid helium are studied. The helium pressure is changed from the saturated vapor pressure to about 25 atm at 1.6 K, under which conditions the liquid helium is in a superfluid state. The pressure shift and broadening of the observed spectra corresponding to the D lines are explained qualitatively by a theoretical calculation based on the spherical atomic bubble model. The Cs D_2 excitation spectra are found to have double peaks, indicating the existence of anisotropic oscillations of the bubble surface. The disappearance of the D_2 emission lines and the pressure-dependent quenching of the Rb D_1 emission lines are also discussed.

PACS number(s): 32.30−r, 32.70.Jz, 67.40.Yv

I. INTRODUCTION

There has been increasing interest in the study of ions and neutral atoms in superfluid helium in the context of atomic physics, condensed-matter physics, low-temperature physics, and also application to elementary particle physics. A large number of experimental and theoretical studies of ions (electron and He^+) in liquid helium have revealed many unique and interesting properties of this quantum liquid and ion structures in liquid: "bubbles" for electrons and "snowballs" for He^+ ions. The bubble is produced by the repulsive force between electrons of impurity and helium due to the Pauli exclusion principle, and the snowball is a cluster of helium atoms with the ion core produced by the charge induced dipole interaction. Recently, the absorption spectra of the electron have been observed in pressurized liquid and solid helium. These spectra have been described successfully within the framework of the bubble model [1]. Spectroscopic research has also been conducted on neutral atoms (metastable helium, alkaline-earth-metal atoms, and alkali-metal atoms) immersed in liquid helium [2–6] and the observed spectra have been compared with theoretical model calculations based on the bubble model. The idea that these impurity atoms form similar bubble structures in liquid helium is well accepted (atomic bubbles) [3,6–8]. The investigation of the optical properties of impurity atoms in this system gives us important information about their structure and also about the density profile of surrounding helium atoms, the dynamics of relaxation and/or nonradiative transitions from the excited states, and the possibility for applications to various fields of fundamental research. Alkali-metal atoms are considered to be the best probe for such research from both experimental and theoretical points of view because of their simple electronic structures and atomic transition lines (D lines) lying in the visible and near infrared regions. Furthermore, optical pumping has been successfully applied to achieve large spin polarization of both electron and nuclear spins of the alkali-metal atoms [9].

In this paper we report on the pressure dependence of the D_1 and D_2 excitation spectra and of the D_1 emission spectra of Cs and Rb atoms, with the pressure P ranging from the saturated vapor pressure [(SVP) 7.4×10^{-3} atm] to ~ 25 atm. The observed pressure dependence of main spectral features (peak shift, broadening, and line shape) are compared with a theoretical calculation based on the spherical atomic bubble model.

In Sec. II we describe the experimental apparatus, the experimental procedure, and the observed excitation and emission spectra at various pressures. In Sec. III the theoretical model used to calculate the energies of atomic bubble states is described, starting from the pair potential method. Numerical results are then given. In Sec. IV, comparing the main spectral features obtained from theoretically calculated energies with experimental results, we discuss peak shift and broadening, and optical line shape and line intensity.

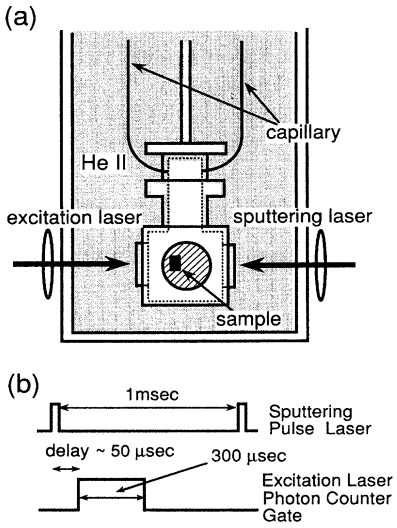

FIG. 1. (a) Experimental apparatus. The beams from a pulse YLF laser for sputtering and an intensity-modulated cw Ti:Al_2O_3 laser for excitation were applied through the windows of the pressure cell. Helium gas was transferred through the stainless steel capillary in order to change the liquid pressure. The setup inside the pressure cell was similar to that in our previous experiments. The photon counting system used to detect the laser-induced fluorescence (LIF) is not shown in the figure. (b) Typical timing chart of sputtering pulse and photon counting gate for the detection of LIF.

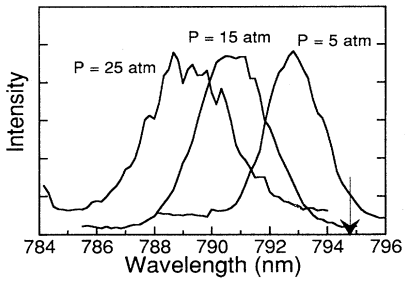

FIG. 2. D_1 emission spectra of Rb atoms excited through the D_1 line at helium pressures of 5, 15, and 25 atm. The intensity at the peak of each line was normalized. The resolution of the monochromator was about 0.5 nm. The arrow shows the position of the D_1 line of a free Rb atom.

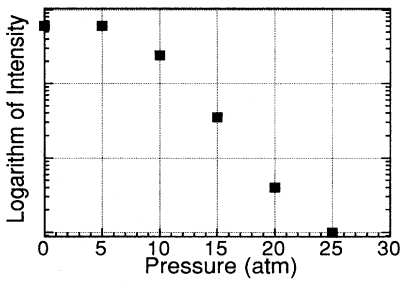

FIG. 3. Intensity of the Rb D_1 emission spectrum as a function of helium pressure. The intensity was measured by tuning the laser wavelength to the peak of the D_1 excitation spectrum.

II. EXPERIMENT

A. Apparatus and procedure

The experimental apparatus is illustrated in Fig. 1(a). The experiment was performed with a stainless steel pressure cell (inner volume ~ 40 cm^3) mounted in a glass Dewar flask filled with superfluid helium (He II) cooled to ~ 1.5 K. We altered the pressure of liquid helium only inside the cell by transferring helium gas through the stainless steel capillary. The equilibrium pressure was measured by a sensor situated outside the Dewar flask. The temperature of liquid helium both inside and outside the pressure cell was monitored with carbon resistors. Cs and Rb atoms were implanted into pressurized superfluid helium using a laser sputtering method [4], in which the Q-switched Nd:YLF($YLiF_4$) laser (wavelength 523 nm, repetition rate ~ 1 kHz, and pulse energy 200 μJ) was focused on the surface of metal samples placed in the cell. The heat energy deposited by the sputtering and excitation lasers caused a non-negligible increase in the liquid temperature because of the small volume of the cell and insufficient thermal conductivity of the stainless steel cell. In order to prevent excessive rise in liquid temperature, we modulated the intensity of the cw Ti:Al_2O_3 laser for excitation (average power $\leq$ 50 mW in front of the glass Dewar flask). During the measurement, the helium temperature inside the cell was ~ 1.6 K, with the pressure change being only a few percent even at high pressure (~ 25 atm). No boiling inside the pressure cell was observed. A typical timing chart is illustrated in Fig. 1(b). We integrated the photon counts of the laser-induced fluorescence (LIF) for ~ 300 μsec with a delay time ~ 50 μsec after the sputtering pulse. Other experimental apparatus (experimental setup inside the cell, monochromator, and photon counting system of the LIF) and procedures were similar to those used in our previous experiments [4,5,9].

B. Experimental results

We could observe the LIF of the D_1 emission line and the D_1,D_2 excitation spectra of Cs and Rb atoms in liquid helium at various pressures from the SVP to ~ 25 atm. The spectral features of Cs and Rb atoms were found to be nearly identical, with the exception of a small number of points. Figure 2 shows the observed Rb D_1 emission lines at several different pressures, where the peak intensities are normalized. In order to obtain such an emission spectrum, we tuned the excitation laser to the center of the D_1 excitation spectrum, which shifted with helium pressure. In Fig. 2 one can see that the emission line is broadened and shifted toward blue with the increase of helium pressure.

The intensities of the Rb D_1 emission lines through the D_1 excitation lines were found to decrease exponentially with the increase of pressure, as shown in Fig. 3. This pressure dependence indicates the existence of quenching at higer helium pressures. Similar strong pressure-dependent quenching was reported in the case of certain metastable helium atomic and molecular transition lines [2]. It was, however, found that the intensities of the Cs D_1 emission lines are not strongly dependent on the helium pressure.

Figures 4(a) and 4(b) show the D_1 and D_2 excitation spectra of Rb and Cs atoms, respectively, both of which were obtained by measuring the intensities of D_1 emission lines. The ratio of peak intensities of the D_1 and D_2 excitation lines of Cs atoms was measured as $\sim$ 10:1 at the SVP and $\sim$ 30:1 in pressurized He II. For Rb atoms the correspond-

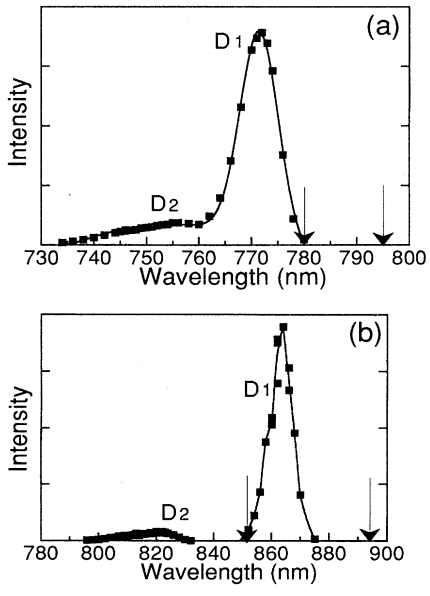

FIG. 4. Observed D_1 and D_2 excitation spectra of (a) Rb atoms at 15.0 atm and (b) Cs atoms at 14.8 atm. These excitation spectra were obtained by detecting the peak intensity of the D_1 emission line while scanning the excitation laser wavelength. The arrows show the positions of the D lines of free atoms.

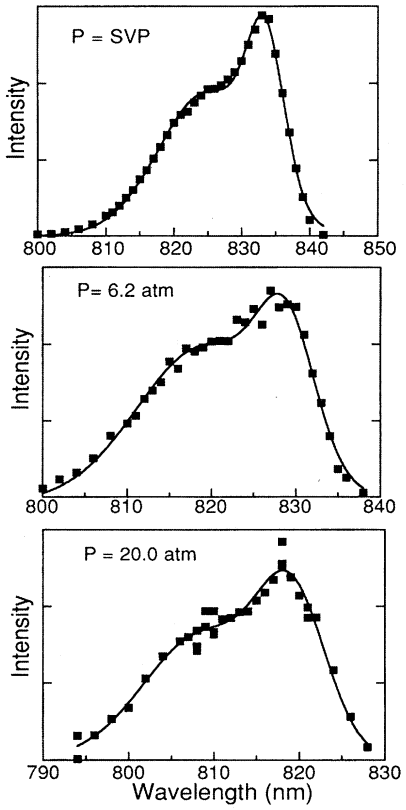

FIG. 5. Cs D_2 excitation spectra at three helium pressures: SVP, 6.2, and 20.0 atm. The experimental spectral profiles were fit using the sum of two Gaussians (solid lines). The values of the fitting parameters are listed in Table I.

ing ratios were found to be $\sim$ 5:1 and $\sim$ 10:1, respectively.

In previous experiments, we observed the Cs D_2 emission line at the SVP with no evident peak shift [5]. The intensity of this line was $\sim$1000 times weaker than that of the D_1 emission line. However, in the present experiment the D_2 emission lines of Cs and Rb atoms could not be detected. The most probable cause of this is the rapid relaxation from the excited $P_{3/2}$ state to the $P_{1/2}$ state. This relaxation takes place over a time much shorter than the radiative lifetime of $P_{3/2}$ state. However, from the observed relative intensity ratio of the D_1 and D_2 excitation lines, we believe that the D_2 emission lines shift significantly toward red and that their wavelengths are out of the detectable range of our detector ($\lambda \lesssim 930$ nm) [10]. Another possibility is that the excited $P_{3/2}$ state partially relaxes to the ground state through a nonradiative process. These points will be discussed again in Sec. IV.D..

The shapes of the observed D_1 emission spectra are symmetric (see Fig. 2), while the shape of the D_1 excitation line is slightly asymmetric. On the other hand, the D_2 excitation spectrum has a shape considerably different from that of the D_1 spectrum. Figure 5 shows the Cs D_2 excitation spectra at various pressures. We found the observed D_2 excitation spectrum to be comprised of two components; the component located on the side of shorter wavelength is broader than that at longer wavelength, as for the D_2 excitation spectrum of Ba^+ ions in He II at the SVP [11]. The line shape

TABLE I. Center wavelengths and widths of the two components of the Cs D_2 excitation spectra at various pressures, obtained by fitting to the sum of two Gaussians. The theoretical results [wavelength at peak and full width at half maximum (FWHM)] of our model calculation are also shown. The experimental uncertainty with all data is ± 0.4 nm.

	Experiment				Theory	
Pressure (atm)	Center (nm)	FWHM (nm)	Center (nm)	FWHM (nm)	Peak (nm)	FWHM (nm)
SVP	833.6	6.3	825.2	17.4	835.2	3.6
6.20	828.9	7.9	819.4	19.2	831.4 [a]	4.0 [a]
9.75	826.4	9.1	815.0	19.4	828.2 [b]	4.3 [b]
14.8	822.8	9.8	813.0	20.2	825.3 [c]	4.6 [c]
20.0	819.2	9.4	808.8	16.4	822.8	4.8

[a]Values calculated at $P = 5.0$ atm.
[b]Values calculated at $P = 10.0$ atm.
[c]Values calculated at $P = 15.0$ atm.

was fit to the sum of two Gaussian curves. The center wavelengths and the widths of the two components are listed in Table I. The observed splitting interval tends to increase with helium pressure. The doubly peaked profile of the observed D_2 spectra indicates clearly the existence of an anisotropic density distribution of surrounding helium atoms. This anisotropy removes the degeneracy of sublevels, as seen in the Jahn-Teller effect in solids. We will discuss this again in Sec. IV.C.

In the case of Rb atoms, splitting in the D_2 excitation spectrum was not obvious [see Fig. 4(a)], but the observed linewidth was too broad to be a single band. We tried to fit the observed data to the sum of two Gaussian curves after eliminating the slight overlap of D_1 excitation lines. The results are shown in Table II. The separation of the two components of the Rb D_2 excitation spectrum is smaller than that of the Cs D_2 spectrum. Furthermore, the overlap of D_1 and D_2 spectra of Rb atoms is larger than that of Cs atoms. These factors may prevent us from clearly observing the structured line shape.

Figures 6(a) and 6(b) show the pressure dependence of the peak shift and broadening of the D_1 emission lines of Cs and Rb atoms, respectively and Figs. 7(a) and 7(b) show the same for the D_1 excitation lines. In Figs. 6 and 7 the theoretical values found using the atomic bubble model are also shown (solid and dashed lines). These are discussed in Sec. III. The observed shifts and broadenings of both excitation and emission spectra increase linearly with helium pressure, at least in the pressure range of the liquid phase.

TABLE II. Same as in Table I, but for the case of the Rb D_2 excitation spectra.

	Experiment			
Pressure (atm)	Center (nm)	FWHM (nm)	Center (nm)	FWHM (nm)
SVP	764.9	6.8	758.1	13.0
5.02	760.7	5.8	757.5	24.4
10.4	758.1	6.9	754.4	22.1
15.0	755.8	4.9	751.8	24.4

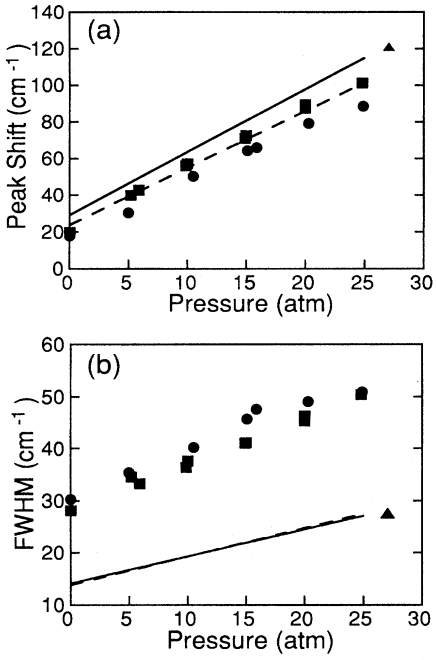

FIG. 6. (a) Pressure shift (blueshift) and (b) broadening of the D_1 emission spectra of Cs and Rb atoms as a function of helium pressure. Solid squares (Cs) and solid circles (Rb) show the experimental results. Solid (Cs) and dashed (Rb) lines represent the theoretical values calculated using the spherical atomic bubble model. Triangles in (a) and (b) show the predicted values for the Cs D_1 line in solid helium just at the freezing point (27.06 atm).

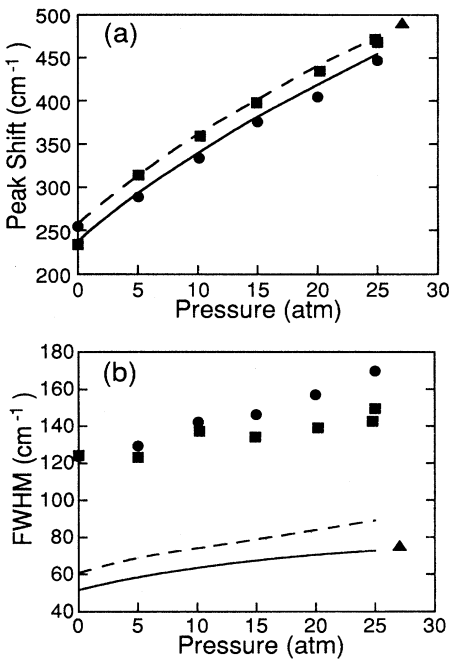

FIG. 7. (a) Pressure shift (blueshift) and (b) broadening of the D_1 excitation spectra of Cs and Rb atoms. The symbols used are the same as those in Fig. 6.

III. MODEL CALCULATION

A. Theoretical model

The system to be studied here is an impurity alkali-metal atom surrounded by a large number of helium atoms. Our theoretical model is based on the fundamental assumption that such an alkali-metal atom exists inside a microscopic cavity in liquid helium, i.e., forming "bubble structure."

We carried out the model calculation for this system in the following manner. We first calculated the components of the pair potential of an alkali metal and a helium atom by using the method developed by Baylis [12,13]:

$$H_{\text{alkali-He}}(\mathbf{r},\mathbf{R}) = H_A(r) + V_I(\mathbf{r},\mathbf{R}), \tag{3.1}$$

where $\mathbf{r}$ and $\mathbf{R}$ are the position vectors of the alkali-metal valence electron and the helium atom relative to the alkali-metal nucleus, respectively, $H_A(r)$ is the valence electron Hamiltonian of the free alkali-metal atom including the spin-orbit interaction, and $V_I(\mathbf{r},\mathbf{R})$ represents the interaction between three bodies, i.e., the frozen alkali-metal core, the frozen helium atom, and the alkali-metal valence electron. Therefore $V_I(\mathbf{r},\mathbf{R})$ comprises three parts

$$V_I(\mathbf{r},\mathbf{R}) = F(\mathbf{r},\mathbf{R}) + G(\mathbf{r},\mathbf{R}) + W(R), \tag{3.2}$$

where $F(\mathbf{r},\mathbf{R})$ is the effective electrostatic interaction between two atoms, whose attractive potential represents well the long-range alkali-metal–helium interaction and takes the van der Waals form at large internuclear distances. This interaction potential can be regarded as the energy of a helium atom having a polarizability α_B and a radius r_0 in an instantaneous electric field $\mathbf{E}(\mathbf{r},\mathbf{R})$ produced by the alkali-metal valence electron and the alkali-metal core:

$$\begin{aligned} F(\mathbf{r},\mathbf{R}) &= -\tfrac{1}{2}\alpha_B[\mathbf{E}(\mathbf{r},\mathbf{R})]^2 \\ &= -\tfrac{1}{2}\alpha_B e^2\left[\frac{\mathbf{R}}{R^3} - \frac{\mathbf{r}'}{r'^3}\right]^2, \quad r_0 \leqslant r \\ &= -\tfrac{1}{2}\alpha_B e^2\left[\frac{1}{R^4} + \frac{1}{r_0'^4}\right], \quad r < r_0, \end{aligned} \tag{3.3}$$

where $\mathbf{r}' = \mathbf{R} - \mathbf{r}$. Here we have used the values α_B = 1.384 in a.u. (cubic bohrs), r_0 = 0.619 a.u. for the Cs-He system, and r_0 = 0.638 a.u. for the Rb-He system [12].

In Eq. (3.2), $G(\mathbf{r},\mathbf{R})$ and $W(R)$ represent the pseudopotentials corresponding to the compensational energies arising due to the lack of orthogonality of the helium atom with the alkali-metal valence electron and the alkali-metal core, respectively. These can be written as

$$G(\mathbf{r},\mathbf{R}) = \frac{\hbar^2}{2m_e}[3\pi^2\rho_B(r')]^{2/3} \tag{3.4}$$

and

$$\begin{aligned} W(R) = \frac{3\hbar^2}{10m_e}[3\pi^2]^{\frac{2}{3}} \int d^3r[\{\rho_A(r) + \rho_B(r')\}^{5/3} \\ - \rho_A{}^{5/3}(r) - \rho_B{}^{5/3}(r')], \end{aligned} \tag{3.5}$$

where m_e is the electron mass and $\rho_A(r)$ and $\rho_B(r')$ are the radial charge distribution densities of the alkali-metal core

and a helium atom, respectively. These terms are repulsive and dominate at small internuclear distances. Baylis [12] and Pascale and Vandeplanque [13] calculated the densities $\rho_A(r)$ and $\rho_B(r')$ using the simplified self-consistent field method of Gombas.

It is convenient to expand $V_I(\mathbf{r},\mathbf{R})$ in terms of spherical harmonics when the potential is summed over all surrounding helium atoms,

$$V_I(\mathbf{r},\mathbf{R})=\sum_{L=0}^{\infty} V_I^{(L)}(r,R)\frac{4\pi}{2L+1} \times \sum_{M=-L}^{L} Y_L^{M*}(\theta,\phi)Y_L^M(\Theta,\Phi), \quad (3.6)$$

where we have used the polar coordinates $\mathbf{r}=(r,\theta,\phi)$ and $\mathbf{R}=(R,\Theta,\Phi)$. In Eq. (3.6), $V_I^{(L)}(r,R)$ is given by the Legendre transformation of $V_I(\mathbf{r},\mathbf{R})$

$$V_I^{(L)}(r,R)=\frac{2L+1}{2}\int_{-1}^{1} d(\cos\eta)V_I(\mathbf{r},\mathbf{R})P_L(\cos\eta), \quad (3.7)$$

where η is the angle between $\mathbf{r}$ and $\mathbf{R}$. Expanding $F(\mathbf{r},\mathbf{R})$ and $G(\mathbf{r},\mathbf{R})$ in a similar form, we obtain

$$V_I^{(0)}(r,R)=F^{(0)}(r,R)+G^{(0)}(r,R)+W(R) \quad (3.8)$$

and, for $L\neq 0$,

$$V_I^{(L)}(r,R)=F^{(L)}(r,R)+G^{(L)}(r,R). \quad (3.9)$$

The expressions for $F^{(L)}(r,R)$ and $G^{(L)}(r,R)$ are given in Refs. [12,13]. Baylis [12] and Pascale and Vandeplanque [13] obtained the alkali-metal–helium pair potential by computing the eigenvalues of the Hamiltonian $H_{\text{alkali-He}}$ using a large number of free alkali-metal atomic eigenstates. We applied this pair potential method to the alkali-metal atom in liquid helium, where the liquid was treated as a continuously distributed medium. Hence the total Hamiltonian H_E can be obtained by weighting with the density profile $\rho(R,\Theta,\Phi)$ of the surrounding helium atoms

$$H_E=H_A(r)+\int \rho(R,\Theta,\Phi)V_I(\mathbf{r},\mathbf{R})d\mathbf{R} =H_A(r)+\int d\mathbf{R}\ \rho(R,\Theta,\Phi)\sum_{L=0}^{\infty} V_I^{(L)}(r,R)\frac{4\pi}{2L+1} \times \sum_{M=-L}^{L} Y_L^{M*}(\theta,\phi)Y_L^M(\Theta,\Phi). \quad (3.10)$$

When the density profile of helium atoms is spherically symmetric, ρ depends only on R, and hence the total Hamiltonian H_E depends on r only. In this case the terms with $L\neq 0$ in the summation in the Eq. (3.10) vanish. However, the density profile can generally be anisotropic and depend on the angular variables, resulting in the reduced symmetry of the total Hamiltonian. Then the higher terms in the Hamiltonian H_E cause mixing of the $|Jm_J\rangle$ state.

We diagonalized this total Hamiltonian in the basis states $|A\rangle|\sigma_Z\rangle$, where $|A\rangle$ represents the lowest four unperturbed alkali-metal states, $|LM_L\rangle(L=1,0)$, and $|\sigma_Z\rangle$ represents spin up and down states. To calculate the radial electronic charge densities $\rho_A(r),\rho_B(r')$ in Eqs. (3.4) and (3.5) and the matrix elements of H_E, we used the wave functions obtained by solving numerically the Schrödinger equation for the alkali-metal valence electron in the atomic potential determined by the Hartree-Fock-Slater self-consistent field method under the frozen atomic core approximation [14]. Thus the eigenenergies are the adiabatic interaction potentials between the impurity alkali-metal atom and surrounding helium atoms.

In this paper we treat the case of a spherical bubble structure for the helium density distribution. We assume that the density profile can be expressed as [15]

$$\rho(R,R_0,\alpha) =\begin{cases} 0, & R<R_0 \\ \rho_0\left[1-\{1+\alpha(R-R_0)\}e^{-\alpha(R-R_0)}\right], & R_0\leq R, \end{cases} \quad (3.11)$$

where ρ_0 is the pressure-dependent number density of liquid helium, R_0 is the bubble radius, and α presents the width of the transition region. The equilibrium bubble radius $R_{0\,\text{eq}}$ and α are determined by minimizing the total energy of this system

$$E_{\text{tot}}(R_0,\alpha)=E_{\text{atom}}+E_{\text{surf}}+E_{\text{PV}}+E_{\text{VK}}, \quad (3.12)$$

where E_{atom} represents the atomic energy in liquid, given by the eigenenergy of Eq. (3.10). The remaining terms represent the classical energies required to form the cavity; E_{surf} is the surface energy given by $4\pi R_b^2\sigma$, E_{PV} is the pressure volume (PV) work given by $\frac{4}{3}\pi R_b^3 P$, and E_{VK} is the volume kinetic energy due to the density gradient at the edge of cavity, which can be expressed as $\hbar^2/(8M_{\text{He}})\int d^3R(\nabla\rho)^2/\rho$ [15]. Here P is the helium pressure, σ is the surface tension, which is known to be 0.327 51 ergs/cm^2 at 1.6 K [16] and is assumed to be independent of the helium pressure, M_{He} is the mass of a helium atom, and R_b is the effective bubble radius defined by the "center of mass" around the region of the cavity edge [7]

$$\int_0^{R_b}\rho(R)4\pi R^2dR=\int_{R_b}^{\infty}[\rho_0-\rho(R)]4\pi R^2dR. \quad (3.13)$$

From Eq. (3.12), the configuration coordinate diagrams with respect to R_0 can be obtained. In particular, we calculated the cases of Cs and Rb atoms in ground and first excited P states for various helium pressures. Here it must be noted that, according to the Franck-Condon principle, the density distribution of surrounding helium atoms does not change during the transition between the ground and excited states. Therefore, for the excitation process, we calculated the energy of the excited states using the same values of R_0 and α as used to determine the total energy of the ground state. Similarly, for the emission process, we used the values of R_0 and α for the atomic bubble in the excited state.

TABLE III. Calculated equilibrium bubble radius R_{0eq}, effective bubble radius R_b, parameter α, and total energy shifts ΔE_S of the ground state $6S_{1/2}$ Cs bubble at the minimum of the total energy and corresponding total energy shifts ΔE_P of the excited $6P$ state at various helium pressures. The relative energy shifts $\Delta E(=\Delta E_P-\Delta E_S)$ are shown in the last column. All listed values are common to the $P_{3/2}$ and $P_{1/2}$ states in our calculation. All energies are in units of 10^2 cm^{-1}.

P (atm)	R_{0eq} (a.u.)	R_b (a.u.)	α (1/a.u.)	ΔE_S	ΔE_P	ΔE
SVP	11.225	13.582	0.92	1.0364	3.4107	2.3743
5.0	11.075	13.189	1.02	1.4153	4.3464	2.9311
10.0	10.975	12.891	1.12	1.7700	5.1638	3.3938
15.0	10.875	12.722	1.16	2.1072	5.9233	3.8161
20.0	10.800	12.522	1.24	2.4317	6.6153	4.1836
25.0	10.725	12.391	1.28	2.7454	7.2880	4.5426
27.06	10.750	12.415	1.28	2.9035	7.8142	4.9107

B. Result of calculation

In Table III we give the calculated pressure dependence of the parameters associated with the Cs atomic bubble, and the total energy shifts (ΔE_S and ΔE_P) of the ground $6^2S_{1/2}$ and excited 6^2P states, respectively, with a bubble size corresponding to that for a system at equilibrium in the ground state. Table IV displays the pressure dependence of the same quantities as those in Table III but with a bubble size corresponding to that for an equilibrium system in the excited P state, i.e., at the moment of light emission. In our nonrelativistic treatment, the radial wave function of the $P_{1/2}$ state is the same as that of the $P_{3/2}$ state. Therefore, under the spherical bubble approximation, the energy difference between these two states is due solely to the spin-orbit interaction.

The "surface thickness," i.e., the transition region $[0.1\leq\rho(R)/\rho_0\leq 0.9]$ at the boundary of the equilibrium bubble, is in the range 1.4–2.4 Å, depending on the pressure. As shown in Tables III and IV, we also see that the equilibrium bubble radius $R_{0\,eq}$ decreases slightly with increasing pressure. The increase of helium pressure causes variation mainly in E_{PV} and E_{atom}. At the SVP, $R_{0\,eq}$ is determined mainly by the perturbed atomic energy E_{atom} and the surface energy E_{surf}. The PV work E_{PV} becomes comparable with E_{surf} at ~ 10 atm and more important in determining $R_{0\,eq}$ at higher pressures. However, compared with the change in liquid density resulting when the pressure is increased from the SVP to 25 atm ($\sim 20\%$), the corresponding change in $R_{0\,eq}$ is quite small ($\sim 5\%$). This contrasts with the case of the electron bubble, which is known to be very compressible. This difference is due to the localized wave functions of the alkali-metal valence electron and the alkali-metal core.

The configuration coordinate diagrams for the Cs ground $6S_{1/2}$ state and the excited $6P_{1/2}$ and $6P_{3/2}$ states at the SVP are illustrated in Fig. 8. The solid and dashed lines in Fig. 8 represent the total energy shifts (ΔE_S and ΔE_P) of the system relative to free atomic states, corresponding to the excitation and emission processes, respectively. The radial wave function of the excited P state extends larger distances from the nucleus than that of the $S_{1/2}$ state. Thus the equilibrium bubble size in the excited state (R_{ex}) is larger than that in the ground state (R_g), as seen in Fig. 8. The potential energy curve of the excited state changes more rapidly with R_0 than that of the ground state in the vicinity of R_g, while the lower potential energy curve is not steep in the vicinity of R_{ex}. Therefore, the blueshifts and broadenings of the excitation lines are larger than those of the emission lines.

We obtained the peak shifts relative to free atomic transition lines, broadenings, and the shapes of optical excitation and emission lines from the calculated configuration coordinate diagrams at various pressures. For the excitation spectra, we approximated the potential energy curve of the ground state in the vicinity of its energy minimum by a harmonic potential and calculated the wave function $\chi_{v=0}$ of the vibronic ground state for bubble surface oscillations. (We confirmed that the potential for lowest five vibronic states, at least, was well approximated by that of a harmonic oscillator.) In the case of a spherical bubble, the bubble oscillations around the equilibrium shape are limited to the breathing modes. We used $4\pi R_b{}^3\rho_0 M_{He}$ as the effective mass for these modes [17]. The typical energy interval between the vibronic states in the electronic ground state $S_{1/2}$ is ~ 4.5 K at the SVP and ~ 6.3 K at 20 atm for Cs atoms. These energy differences are larger than the thermal energy at the tempera-

TABLE IV. Same as in Table III, but for the case of a $6P$ Cs bubble at the minimum of the total energy. All energies are in units of 10^2 cm^{-1}.

P (atm)	R_{0eq} (a.u.)	R_b (a.u.)	α (1/a.u.)	ΔE_P	ΔE_S	ΔE
SVP	13.950	16.878	0.74	1.9086	1.6310	0.2777
5.0	13.700	16.139	0.88	2.6341	2.1726	0.4615
10.0	13.475	15.702	0.96	3.2947	2.6476	0.6471
15.0	13.300	15.391	1.02	3.9133	3.0939	0.8194
20.0	13.175	15.145	1.08	4.5012	3.5256	0.9756
25.0	13.050	14.912	1.14	5.0650	3.9289	1.136
27.06	13.075	14.972	1.12	5.3936	4.1834	1.210

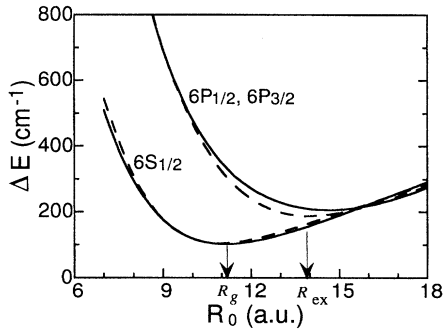

FIG. 8. Shift of the total energies of a Cs atomic bubble in the $6S_{1/2}$, $6P_{1/2}$, and $6P_{3/2}$ states relative to corresponding free atomic energies as a function of the bubble radius R_0 at SVP. Solid and dashed lines represent the excitation and emission process, respectively. R_g and R_{ex} represent the equilibrium bubble radii in the ground $S_{1/2}$ and excited P states, respectively. Under the assumption of the spherical atomic bubble, the total energy shifts for the $P_{3/2}$ and $P_{1/2}$ states are the same.

ture in our experiments (1.6 K). Therefore, we can safely assume that only the vibronic ground state ($v=0$) is populated at thermal equilibrium. The excitation spectra were obtained by projecting the probability density $|\chi_{v=0}|^2$ to the potential energy curve of excited states (as in Ref. [3]), under the assumption that the electronic dipole moment is independent of R_0. The same method was used to calculate the emission spectra of Cs atoms and the excitation and emission spectra of Rb atoms.

We have, to this point, implicitly used the Born-Oppenheimer approximation for the valence electron motion and the bubble surface oscillation. It is worthwhile to consider the validity of this approximation. In our case, the parameter to determine the validity of adiabatic treatment [18,19] is the ratio between the electron mass (m_e) and the effective mass for the breathing modes

$$\kappa=\left(\frac{m_e}{4\pi R_b{}^3\rho_0 M_{\mathrm{He}}}\right)^{1/4}, \tag{3.14}$$

which is typically ~ 0.04. This small value of κ implies that the bubble surface oscillations are almost stationary during a period of electron motion. Furthermore, the breathing modes, which preserve the spherical symmetry of the system, do not remove the degeneracy of the excited states and do not cause transitions between electronic states. Therefore, the bubble surface oscillations can be regarded as being adiabatic with respect to electron motion.

In our theoretical calculation, we have introduced additional assumptions and approximations, resulting in a certain amount of error. In particular, we have ignored the interaction between helium atoms. In addition, the concepts of surface energy and PV work, which, strictly speaking, are valid only in macroscopic systems, have been applied to the microscopic atomic bubble (with size on the order of the atomic radius). Further, the effective mass m_{eff} has been derived with the assumption that the liquid is incompressible [17]. Finally, the values assumed for the polarizability α_B and a dipole radius r_0 [appearing below Eq. (3.3)] are only approximate.

IV. DISCUSSION

A. Line shift

The theoretical results for the pressure dependence of peak shifts of the D_1 emission spectra of Cs and Rb atoms are shown in Fig. 6(a) together with the experimental results. The pressure shifts of the D_1 excitation spectra of these atoms are shown in Fig. 7(a). As seen in Figs. 6(a) and 7(a), quantitative agreement between the theoretical and experimental shifts of both D_1 excitation and emission lines is satisfactory.

The theoretical shifts and broadening (in energy units) of the D_2 spectra are essentially the same as those of the D_1 lines, as mentioned above. Apart from the discrepancy with respect to the line shape and linewidth of the D_2 excitation lines, the wavelengths at the peak of the D_2 excitation lines predicted by the spherical bubble model are in qualitative agreement with the wavelengths at the peak of the stronger component of the observed spectra (see Table I).

Both the experimental and theoretical results show that the (blue) peak shifts are approximately proportional to helium pressure, at least in the range of the liquid phase. The number density of helium atoms increases linearly with the pressure in the liquid phase. When the pressure is increased and crosses the phase transition point from liquid to solid, the number density jumps about 10%. Altering our model only by changing the number density by this amount, we calculate the shifts and broadenings of the D lines of Cs atoms in solid helium just at the freezing point ($P=27.06$ atm and $T=1.6$ K). The results are expressed by triangles in Figs. 6 and 7. Although the distinction between the broadening and shift of the emission lines in liquids and in solids is not clear, the jump in the shift of the excitation line is of detectable size. It is important to measure this jump experimentally in order to know whether the fundamental concepts used in our theoretical model can also be applied to the solid phase [20].

B. Linewidth

The theoretical pressure broadening of the D_1 emission and excitation lines is shown in Figs. 6(b) and 7(b), respectively, together with the experimental results. The measured linewidths for all spectra are about twice as large as the calculated values. It should be noted, however, that the slope of the pressure broadening agrees well with the results of model calculation.

To obtain quantitative agreement with respect to the linewidth, we must take account of additional effects. First, it is important to obtain better estimates for our model potential. The components of the model potential we have used, in particular, the slope of the repulsive part, may be underestimated in our calculation. Second, in our method, the linewidths change with the effective mass m_{eff} for the breathing modes through the broadening of the density distribution $|\chi_{v=0}|^2 \propto \sqrt{2\hbar/m_{\mathrm{eff}}\omega} \propto m_{\mathrm{eff}}^{-1/4}$. Here ω is the frequency for the breathing mode. A steeper repulsive part of the adiabatic potentials and smaller effective mass m_{eff} will cause a larger line broadening and asymmetric line shape. Third, we must treat the transitions more quantum mechanically to estimate preseise linewidths and line shapes; the Franck-Condon fac-

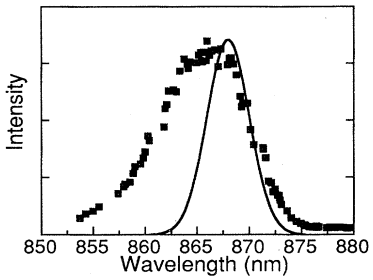

FIG. 9. Observed and calculated shapes of the Cs D_1 excitation spectrum at a helium pressure of 10.0 atm are shown by solid squares and a solid line, respectively.

tors should be calculated [3]. In addition, the lifetimes of vibronic states of the electronic excited states, which we have ignored, must be considered. These lifetimes are expected to be very short due to rapid relaxation to the lowest vibronic state and are considered to be given approximately by the time required for the bubble to expand from its equilibrium size in the ground state to that in the excited state. If we assume that the expansion occurs at the sound velocity, which is in the range 200–400 m/sec depending on the temperature and pressure [21], the expansion time becomes roughly $\sim$ 1 psec. Thus we believe that the relaxation in the excited state contributes to the line broadening to some extent. Furthermore, higher-order bubble surface oscillations, such as quadrupole oscillations, which remove the degeneracy of the excited states m manifolds, may contribute to the linewidths [1,19].

C. Line shape

Figure 9 shows the calculated and observed shapes of the Cs D_1 excitation lines at 10 atm. As seen in Fig. 9, the observed shapes of the D_1 excitation spectra are nearly symmetric, but assume slightly larger values in the short-wavelength tail as compared to the long-wavelength tail. In contrast, similar asymmetric excitation and absorption spectra were observed in the cases of electrons, metastable helium atoms, Ba^+ ions, and the alkaline-earth-metal atoms and these spectral profiles were explained by appealing to the slope of the potential curve of the excited state above the vicinity of the potential minimum of the ground state in the configuration coordinates diagrams [1–3,6,7,11,20]. Our theoretical results show more symmetric profiles for all optical spectra. The discrepancy in the line shapes between the model calculation and experimental results are believed to be attributable to the causes discussed in the previous subsection.

As opposed to the case of D_1 excitation spectra, the observed D_2 excitation spectra are considered to be a superposition of two components. These line shapes cannot satisfactorily be explained with the spherical bubble model. As shown in Table I, the splitting of the two observed components becomes larger at higher pressures. This indicates that the cause of the splitting is strongly related to the surrounding helium atoms. We believe that this structured profile originates in the anisotropic density distribution of surrounding helium atoms, similar to the Jahn-Teller effect in solids. The angular distribution of the wave functions for the $P_{3/2}$ states are highly asymmetric. For the $m_J = \pm 1/2$ substates, the wave functions are prolate, while for the $m_J = \pm 3/2$ substates, they are nearly oblate. It is possible that bubble deformations exist in the form of quadrupole-type oscillations around the equilibrium shape. The reduced symmetry of the Hamiltonian resulting from such bubble surface oscillations leads to the lifting the degeneracy of sublevels of the $P_{3/2}$ states and the splitting of the D_2 excitation spectrum into two components through the Jahn-Teller effect. The D_1 excitation spectra, contrastingly, do not have such a splitting structure. Similar splitting was observed in the excitation spectra of Ba^+ ions in He II [11] and in the absorption spectra of alkali-metal atomic D lines in other rare gas matrices (Ar, Kr, and Xe). The latter phenomenon was explained satisfactorily in terms of the vibronic coupling model involving the Jahn-Teller effect [22]. As suggested in Refs. [11,23], it is not surprising that the Jahn-Teller effect exists even in the case of alkali-metal atoms immersed in liquid helium. We are attempting to interpret this line shape in terms of the Jahn-Teller effect, using a deformed atomic bubble model in which ρ and R_0 include angular variables. The preliminary results show qualitative agreement between the shape of observed Cs D_2 excitation spectra [24]. The details of this study will be discussed elsewhere.

D. Intensity

As mentioned in the Sec. II.B., it was found experimentally that the surrounding liquid strongly influences the relative intensities of the D_1 and D_2 lines in both excitation and emission spectra. The extremely weak D_2 emission lines can be explained partially by fast relaxation from the $P_{3/2}$ state to the $P_{1/2}$ state. If only such fine structure relaxation is induced, the relative intensities of the D_1 and D_2 excitation lines, both measured by detecting the D_1 emission intensity, must be nearly equal to those of the absorption lines, i.e., the ratio for free atoms (1:2). However, the intensity of the D_2 excitation line observed experimentally is much weaker than that of the D_1 line, as seen in Fig. 4. We do not fully understand the cause of this peculiar phenomenon in the present stage. As discussed below, two possible causes can be considered. One is an extremely large shift of the D_2 emission line to the undetectable infrared region in our present experiment. The other is quenching by a radiationless process from the excited $P_{3/2}$ states to the ground $S_{1/2}$ state. The latter, however, is unlikely.

The oscillator strengths for the D excitation lines are affected by the surrounding helium atoms. However, it is unreasonable that only D_2 excitation lines are greatly affected by the helium atoms and thereby made weak in comparsion with the D_1 lines. Because the equilibrium bubble shape in the ground state is almost spherical and does not change during the transition, the perturbations due to the surroundings applied to the excited states $P_{3/2}$ and $P_{1/2}$, which have almost identical electronic radial wave functions, cannot be significantly different.

With respect to the emission process, it is clear that the equilibrium helium distribution around an alkali-metal atom in a P state is for the most part determined by the density spatial distribution of the valence electronic wave function of this P state. Particularly for the $P_{3/2}$, $m_J = \pm 3/2$ and

$P_{3/2}$, $m_J = \pm 1/2$ substates, helium atoms can approach the alkali-metal core easily from the region where the alkali-metal core is relatively unshielded and then the bubble shape is deformed from a sphere. Such an effect may become stronger for higher pressures and cause the pressure-dependent quenching, as suggested by Steets *et al.* [8]. The deformation of the bubble shape reduces the energy of the $P_{3/2}$ states and greatly increases that of the ground $S_{1/2}$ state, possibly resulting in a radical redshift of the D_2 lines. As an extreme case, it is possible that these energy levels cross each other, resulting in a radiationless transition to the ground state. In addition, such an anisotropic deformation mixes fine structure levels and induces the relaxation from the $P_{3/2}$ state to the $P_{1/2}$ state [25]. The interaction of helium atoms with the inner core of the alkali-metal atom increases in this anisotropic configuration. This may alter the oscillator strength of the D_2 emission lines. However, it is not reasonable that the oscillator strength is reduced to less than $\sim 10^{-3}$.

In contrast, while the probability density of the $P_{1/2}$ state wave function is also asymmetric, this asymmetry is not very large and the cusp region where helium atoms can approach the inner core is relatively small. Therefore, the spherical bubble model can be considered to be a good approximation for the $P_{1/2}$ state and the D_1 emission lines do not suffer a severe change due to quenching.

It must, however, be noted that the measured intensity of the Rb D_1 emission line decreased exponentially with increasing pressure, although no apparent decrease of the intensity was observed in the case of the Cs D_1 line. Observed small peak shifts of the Rb D_1 emission lines indicate that the change of the wave function of the $P_{1/2}$ state due to the surrounding helium atoms is very small. As the result, there is no significant reduction of the oscillator strength. Therefore, it is reasonable to believe that, for Rb atoms, there exists another process in which the $P_{1/2}$ state decays to the ground state in addition to the D_1 light emission process. Recently, Dupont-Roc pointed out that, in the case of light alkali-metal atoms, which generally have a small fine structure splitting, the $P_{1/2}$ and $P_{3/2}$ states are significantly mixed by the interaction with helium atoms and hence the angular states of these excited states are described well by the orbital quantum number L rather than J. The lowest energy state in the excited P state is the P_z state and the optimum bubble shape for the P_z state becomes highly anisotropic compared with heavier alkali metals possessing a large fine structure splitting. As a result, a greater number of helium atoms can approach the inner core and the energy levels of the P_z state and ground state approach each other, as discussed by Dupont-Roc [25]. He suggested the possibility of a radiationless transition to the ground state. This effect can, of course, be expected to become larger when the helium pressure is increased. We believe that such a radiationless process, or perhaps a radiative transition at the wavelength in the infrared region, occurs even for Rb atoms in the $5P$ state.

The measurement of the pressure dependence of the decay time of the Rb D_1 emission line is now underway in our laboratory. This may lead us to a comprehensive understanding of the dynamics of the light and heavy alkali-metal atoms.

V. CONCLUSION

In the present paper we have reported the observation of the excitation and emission spectra of Cs and Rb atoms in pressurized liquid helium. Particular attention has been given to the pressure dependence of the D lines of these atoms. It was found experimentally that the shifts and broadenings of the excitation and emission spectra were linearly dependent on the helium pressure over a wide range from the SVP to ~ 25 atm, in which helium was in the superfluid state. To explain the pressure shifts and broadenings, we calculated the energies of the alkali-metal atoms in the ground state and in the first excited P states, using the spherical atomic bubble model. In this calculation, the interaction of an alkali-metal atom with the liquid helium was modeled by applying the pair potential method in which the alkali-metal atom is assumed to interact pairwise with the large number of helium atoms by which it is surrounded. Although there exists a discrepancy between the observed and predicted linewidths, it is noteworthy that such a simplified theory could reproduce even quantitatively the experimentally obtained linearity in the pressure dependence of the shift and broadening of the D lines. This fact strongly supports the fundamental concepts involved in the atomic bubble model. We have also studied other optical properties from the optical line shapes and line intensities. The doubly shaped profiles of the D_2 excitation spectra, which cannot be interpreted with the spherical bubble model, suggest the existence of quadrupole-type bubble surface oscillations removing the degeneracy of the $P_{3/2}$ substates, as in the Jahn-Teller effect. Such an anisotropic density distribution of the surrounding helium atoms, which is expected in equilibrium for the excited P state, may also be closely related to the relaxation and quenching in the excited states. The disappearance of the D_2 emission line and the peculiar intensity ratio of the D_1 and D_2 excitation spectra imply that, in addition to rapid relaxation between fine structure levels, there exists an additional path from the $P_{3/2}$ state to the ground state, a radiationless process, or a radiative transition at a wavelength longer than those detectable with our photon counting system. The pressure-dependent quenching of the Rb D_1 emission line also suggests the existence of such an additional path. At present, we do not know by what process this path is opened. It can, however, be said that the dynamics of the excited P states are determined by the distribution of surrounding helium atoms and particularly by the number of helium atoms that can approach the inner core through the region of small electron density of the P state electron wave functions.

ACKNOWLEDGMENTS

We would like to thank Professor T. Mizusaki for his helpful experimental advice and Professor J. Dupont-Roc for sending us a copy of his work prior to publication. This work was partially supported by the Grant-in-Aid for Scientific Research (04554010), SCAT, Matuo Foundation, and Kurata Foundation. One of the authors (T.K.) acknowledges the financial support of the Japan Society for the Promotion of Science for Young Scientists and the permission to use the computer facilities of laboratory for elementary particles and nuclei at Kyoto University.

[1] C. C. Grimes and G. Adams, Phys. Rev. B **41**, 6366 (1990); B **45**, 2305 (1992); A. Ya. Parshin and S. V. Pereversev, Zh. Eksp. Teor. Fiz. **101**, 126 (1992) [Sov. Phys. JETP **74**, 68 (1992)]; S. V. Pereversev and A. Ya. Parshin, Physica B **197**, 347 (1994); A. I. Golov and L. P. Mezhov-Deglin, Pis'ma Zh. Eksp. Teor. Fiz. **56**, 527 (1992) [JETP Lett. **56**, 514 (1992)].

[2] F. J. Soley and W. A. Fitzsimmons, Phys. Rev. Lett. **32**, 988 (1974).

[3] H. Bauer, M. Beau, B. Friedl, C. Marchand, K. Miltner, and H. J. Reyer, Phys. Lett. A **146**, 134 (1990); G. zu Putlitz and M. R. Beau, *Dye Laser: 25 Years*, edited by M. Stuke, Topics in Applied Physics Vol. 70 (Springer, Berlin, 1992).

[4] A. Fujisaki, K. Sano, T. Kinoshita, Y. Takahashi, and T. Yabuzaki, Phys. Rev. Lett. **71**, 1039 (1993).

[5] Y. Takahashi, K. Sano, T. Kinoshita, and T. Yabuzaki, Phys. Rev. Lett. **71**, 1035 (1993).

[6] J. H. M. Beijersbergen, Q. Hui, and M. Takami, Phys. Lett. A **181**, 393 (1993).

[7] A. P. Hickman, W. Steets, and N. F. Lane, Phys. Rev. B **12**, 3705 (1975).

[8] W. Steets, A. P. Hickman, and N. F. Lane, Chem. Phys. Lett. **28**, 31 (1974).

[9] T. Kinoshita, Y. Takahashi, and T. Yabuzaki, Phys. Rev. B **49**, 3648 (1994).

[10] This limit is due to the sensitivity of a photomultiplier tube used in our photon counting system.

[11] H. J. Reyher, H. Bauer, C. Huber, R. Mayer, A. Schafer, and A. Winnacker, Phys. Lett. A **115**, 238 (1986).

[12] W. E. Baylis, J. Chem. Phys. **51**, 2665 (1969).

[13] J. Pascale and J. Vandeplanque, J. Chem. Phys. **60**, 2278 (1974).

[14] F. Hermann and S. Skillman, *Atomic Structure Calculation* (Prentice-Hall, Englewood Cliffs, NJ, 1963).

[15] K. Hiroike, N. R. Kestner, S. A. Rice, and J. Jortner, J. Chem. Phys. **43**, 2625 (1965).

[16] M. Iino, M. Suzuki, and A. J. Ikushima, J. Low. Temp. Phys. **60**, 155 (1985).

[17] W. B. Fowler and D. L. Dexter, Phys. Rev. **176**, 337 (1968).

[18] M. Born and J. R. Oppenheimer, Ann. Phys. (Leipzig) **84**, 457 (1927).

[19] P. B. Lerner, M. B. Chadwick, and I. M. Sokolov, J. Low Temp. Phys. **90**, 319 (1993).

[20] S. I. Kanorsky, M. Arndt, R. Dziewior, A. Weis, and T. W. Hänsch, Phys. Rev. B **49**, 3645 (1994); **50**, 6296 (1994), observed the optical spectra of the Ba atoms in solid helium.

[21] K. R. Atkins and R. A. Stasior, Can. J. Phys. **31**, 1156 (1953).

[22] W. Weyhmann and F. M. Pipkin, Phys. Rev. **137**, A490 (1965); B. Meyer, J. Chem. Phys. **43**, 2986 (1965); M. McCarty, Jr. and G. W. Robinson, Mol. Phys. **2**, 415 (1959); J. Hormes and J. Schiller, Chem. Phys. **74**, 433 (1983); H. Kuppelmaier, H. J. Stöckmann, A. Steinmetz, E. Görlach, and H. Ackermann, Phys. Lett. **98A**, 187 (1983); C. Samet, J. L. Rose, P. N. Schatz, and M. C. M. O'Brien, Chem. Phys. Lett, **159**, 567 (1989).

[23] M. Himbert, A. Lezama, and J. Dupont-Roc, J. Phys. **46**, 2009 (1985).

[24] T. Kinoshita, K. Fukuda, Y. Takahashi, and T. Yabuzaki, Z. Phys. B (to be published).

[25] J. Dupont-Roc, Z. Phys. B (to be published). This paper shows that, in the case of the Cs $6P_{3/2}$, $m_J = \pm 3/2$ states, only two helium atoms approach the alkali-metal core and shift the D_2 emission line toward red by amount $\sim$ 2000 cm^{-1} (resulting wavelength ~ 1 μm). Therefore, according to his model, a nonradiative transition to the ground state is unlikely to occur for this case. However, the effect of these atoms is sufficient to produce an effective coupling between fine structure levels, which induces fine structure relaxation. On the other hand, in the case of the Na $3P_z$ state, five or six helium atoms can approach the inner core.

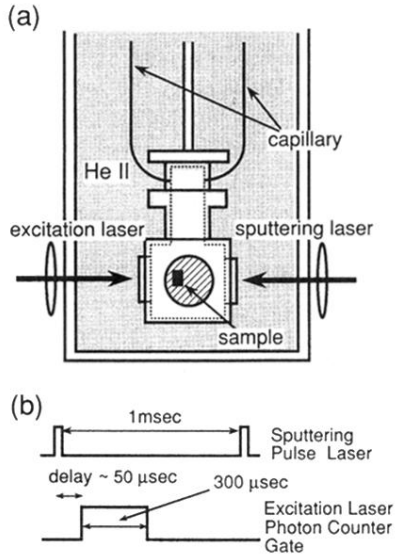

FIG. 1. (a) Experimental apparatus. The beams from a pulse YLF laser for sputtering and an intensity-modulated cw Ti:Al_2O_3 laser for excitation were applied through the windows of the pressure cell. Helium gas was transferred through the stainless steel capillary in order to change the liquid pressure. The setup inside the pressure cell was similar to that in our previous experiments. The photon counting system used to detect the laser-induced fluorescence (LIF) is not shown in the figure. (b) Typical timing chart of sputtering pulse and photon counting gate for the detection of LIF.